



Collimating micro-lens fiber array for noncontact near-infrared diffuse correlation tomography

SHIJIE FENG, ZHIGUO GUI, XIAOJUAN ZHANG, AND YU SHANG* 

Shanxi Provincial Key Laboratory for Biomedical Imaging and Big Data, North University of China, No. 3 Xueyuan Road, Taiyuan 030051, China

*yushang@nuc.edu.cn

Abstract: Near-infrared diffuse correlation spectroscopy/tomography (DCS/DCT) has recently emerged as a noninvasive measurement/imaging technology for tissue blood flow. In DCT studies, the high-dense collection of light temporal autocorrelation curves ($g_2(\tau)$) via fiber array are critical for image reconstruction of blood flow. Previously, the camera-based fiber array limits the field of view (FOV), precluding its applications on large-size human tissues. The line-shape fiber probe based on lens combination, which is predominantly used in current DCT studies, requires rotated-scanning over the surface of target tissue, substantially prolonging the measurement time and increasing the system instability. In this study, we design a noncontact optical probe for DCT based on collimating micro-lens fiber array, termed as FA-nc-DCT system. For each source/detector fiber, a single optical path was collimated by coupling with one micro-lens in the fiber array that is integrated in a square-shape base. Additionally, an 8×8 optical switch is used to share the hardware laser and detectors without spatial scanning. The FA-nc approach for the precise collection of $g_2(\tau)$ curves was validated through a speed-varied phantom experiment and the human experiments of cuff occlusion, from which the expected value of the blood flow index (BFI) was obtained. Furthermore, the flow anomaly in the phantom and the ischemic muscle in human were accurately reconstructed from the FA-nc-DCT system, which is combined with the imaging framework based on the Nth-order linear algorithm that we recently created. Those outcomes demonstrated the great potential of FA-nc-DCT technology for fast and robust imaging of various diseases such as human breast cancers.

© 2021 Optical Society of America under the terms of the [OSA Open Access Publishing Agreement](#)

1. Introduction

The blood flow measurement at microvasculature level is of importance for the diagnosis and treatment of many diseases [1,2], because malfunction of tissues are often associated with abnormal hemodynamics and metabolism. Near-infrared (NIR) diffuse correlation spectroscopy/tomography (DCS/DCT) is a relative new technology for deep tissue blood flow measurement/imaging [3–14]. Due to the relatively low tissue absorption at “NIR window” (650 to 900 nm), DCS/DCT provides a non-invasive, fast, portable, and low-cost alternative for assessing the time course of tissue blood flow changes or spatially localizing the flow anomaly. DCS used one or a few source-detector (S-D) pairs to collect the light temporal autocorrelation curve ($g_2(\tau)$), from which the time-course blood flow index (BFI) can be extracted by fitting the autocorrelation data with an analytical solution of correlation diffusion equation [5,15]. Generally, a near-infrared laser with long-coherence length (>5 m) is used as DCS light source. The avalanche photodiode (APD) single-photon-module is used as the DCS detector, in order to ensure the high sensitivity for probing the fluctuation of individual speckle. By extending DCS to tomography (DCT), which requires a large number of S-D pairs to form a fiber-array, the reconstructed 3D image of blood flow can be obtained.

More often, DCS collects the photon signals via the contact fiber probe, i.e., the optical fibers are placed on the tissue surface [15,16]. This contact pattern of measurement is easy to perform and little affected by the motions and ambient light. However, the contact pressure would cause tissue deformation and cannot be used for ulcer and infectious tissues. It was reported that a few of diseases, such as breast tumors and wounds, are not suitable for measurement with contact probes [7,10,14]. Numerous efforts have been made on the noncontact DCS/DCT measurements by use of lenses to collimate and focus the optical paths on the tissue surface, especially for the DCT system. At the early stage, a single camera lens was shared by source-detector array for light collimation and focus. However, this design limits the field of view (FOV) to 10 mm, only feasible for BFI imaging of small tissues such as mouse or rat brains [8,9]. Enlarging the FOV with a single lens would elevate the effects of optical aberration, causing light interferences between the sources and detectors. To overcome this limit, a line-shape probe was designed for DCS measurements, in which independent lens are used to separate the source and detector path respectively [17]. Extending the DCS to DCT for more signal acquisitions was implemented by the rotated scanning of line-shape probe over the target tissue [11]. The pattern of line-shape scanning permits BFI imaging of relatively large human tissue, and it has been used for breast tumor imaging [18]. However, the optical signals collected via line-scanning mode is susceptible to motion artifacts and remarkably prolongs the signal acquisition time. Moreover, the separation of source light paths and detector light paths with independent lens restricts the positioning of sources and detectors (i.e., line-shape only), making it impossible for flexible design and optimization of source-detector array. Recently, a new imaging system for DCT (termed as speckle contrast diffuse correlation tomography-scDCT) was developed [10,19]. A few approaches have been adopted to replace the line-scanning DCT system. For instance, the introduction of galvanometer-based optical scanning system permits fast scanning of the target area [20–23]. Furthermore, instead of using the APDs, the scDCT adopts an electron-multiplying CCD (EM-CCD) camera as detector. Owing to millions of pixels contained in the CCD camera, the source-detector pairs in the array are substantially increased, allowing for fast sampling rate of DCT imaging. Despite the merits, the sensitivity of EM-CCD to probe individual speckle is far less than that of APD, subsequently affecting the DCT image quality. It is reported that the high quality of scDCT imaging cannot be ensured when the source-detector separation is larger than 1.0 cm [19].

In this study, a new imaging scheme of source-detector array for DCT is created. Specifically, a noncontact optical probe based on collimating micro-lens fiber array, termed as FA-nc system, is designed by us. For each source/detector fiber, a single optical path was collimated by coupling with one micro-lens in the fiber array that are integrated in a square-shape base. Additionally, an 8×8 optical switch is used to share the hardware laser and detectors without spatial scanning. Compared with the single camera and line-shape scanning system that were used previously, this new design minimizes the light interference between the sources and detectors. Additionally, the micro-lens fiber array allows for flexibly positioning individual source/detector fibers over the tissue surface. The flexible S-D configuration is essential for computational optimization of image reconstruction, which, for this study, was implemented by the Nth-order linear (NL) algorithm that were recently proposed by our laboratory [12].

To validate the FA-nc system for precise collection of $g_2(\tau)$ curves, we conducted speed-varied phantom experiment and the human experiments of cuff occlusion, from which the expected value of blood flow index (BFI) were obtained with the DCS solution. These outcomes were further verified by comparison with the conventional contact DCS probe that are believed to have minimal light source-detector interference as well as ambient light effect. Finally, the FA-nc-DCT system, along with the NL algorithm, were used for BFI imaging of liquid phantom and human arm muscles, with the aim to reconstruct flow changes that was intentionally manipulated for system validation.

2. Methods

2.1. Hardware system

The whole system of FA-nc-DCT is illustrated in Fig. 1(a). The system is composed of a long coherence laser at 785 nm (DL-785-120-SO, Crystallaser, Inc., USA) as light source, 6 APD single-photon modules (SPCM-780-13-FC, Excelitas Inc. Canada) as light detectors, an eight-channel digital correlator (correlator.com, USA) and an A/D board (USB-6009, National Instrument Inc., USA) for data acquisition. All these components are contained in an instrument box. To share the source/detector hardware among multiple locations over tissue surface, an 8×8 channel optical switch was designed [Fig. 1(a)]. By using the optical switch, the light from the laser or to the 6 APDs were guided via fiber-array sequentially on specific locations (i.e., a source location and 6 detector locations at one time). In this way, a total of 6×8 array is achieved through 8 times of light switching, resulting in 48 S-D measurements. Figure 1(b) shows the fiber connections on the frontal panel of optical switch. The leftmost column represents the fibers connected to hardware laser/APDs, and the other 8 columns represents the fibers connect to 8 sets of S-D pairs over the FA-nc probe, labeled from Ch1 through Ch8. In the leftmost column, the blue fiber is connected to the laser, and the yellow fibers are connected to the six APDs respectively. When being switched, the light from/to the laser/APDs are distributed into a set of S-D pairs (including one source location and six detector locations), lasting for 1 second. During this period, the laser emits the light into the source location, and the escaping light from six detector locations were collected simultaneously, termed as one cycle of measurement. Once a cycle of measurement is completed, the light is switched to another set of S-D pairs, in sequential manner (i.e., Ch1, Ch2, . . . , Ch8). As such, the emitting/escaping light would cover the entire region of FA-nc probe after 8 times of switching. The specific arrangement for each set of S-D pairs is illustrated in Table 1 and Fig. 4(b). Figure 1(c) depicts a single collimating micro-lens fiber as well as the fiber array on FA-nc probe. The single collimating micro lens fiber (namely, c-lens fiber, Huaxin Inc., China) has the lens length of 1.0 cm and diameter of 2.8 mm. An inclined plane at 8-degree angle is selected to collimate the beam that is delivered via the fiber. With focal length of 50 mm and numerical aperture (NA) of 0.37, this c-lens would achieve good outcomes of light collimating at relatively lower cost. In addition, each collimating micro-lens is coated with a near-infrared anti-reflection film to reduce the influence from ambient light and the reflected light during the experiments.

Table 1. The labels for 8 sets of source-detector (S-D) pairs. Each set of S-D pairs corresponds to each channel of fiber ports on the frontal panel of optical switch

Set 1	Set 2	Set 3	Set 4	Set 5	Set 6	Set 7	Set 8
S1	S2	S3	S4	S5	S6	S7	S8
D11	D21	D31	D41	D51	D61	D71	D81
D12	D22	D32	D42	D52	D62	D72	D82
D13	D23	D33	D43	D53	D63	D73	D83
D14	D24	D34	D44	D54	D64	D74	D84
D15	D25	D35	D45	D55	D65	D75	D85
D16	D26	D36	D46	D56	D66	D76	D86

Figure 2 shows the schematic diagram of the optical paths with the uses of collimating micro-lens fiber and the ordinary fiber (i.e., without collimating). Theoretically, the use of micro-lens can effectively collimate the divergent beam and minimize the spot size, while the light transmission from ordinary fiber would be severely diffused [Fig. 2(a)]. These theories are confirmed through the spot sizes that were actually measured from ordinary fiber and a collimating micro-lens fiber at a working distance of 3 cm [Fig. 2(b)]. As such, the light output from the

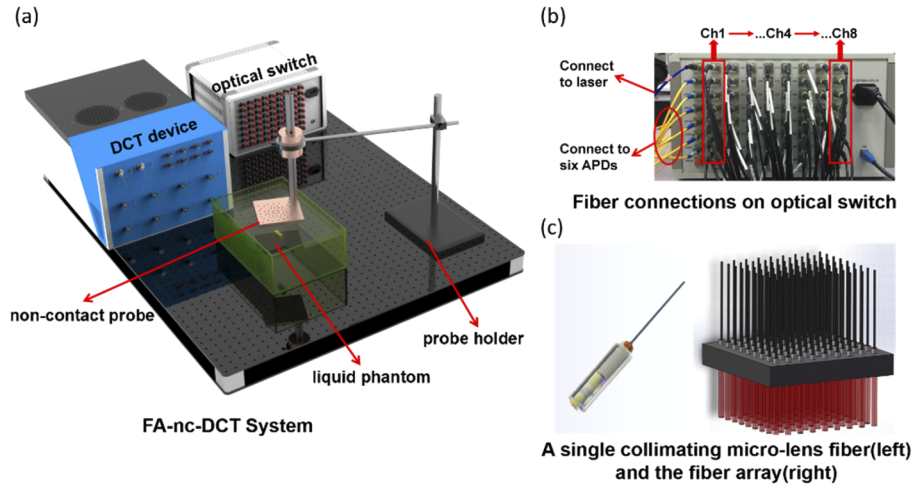


Fig. 1. (a) FA-nc-DCT system, including DCT device, optical switch, noncontact probe, probe holder and liquid phantom. (b) Fiber connections on frontal panel of optical switch. (c) A single collimating micro-lens fiber(left) and the fiber array on FA-nc probe(right), on which the fibers and the collimated light are indicated in black and red respectively.

collimating micro-lens fiber will be focused on the surface of phantom or tissue [Fig. 2(d)], similar to the light transmission by the contact fiber probe [Fig. 2(c)]. Note that Figs. 2(c) and 2(d) only represent the schematics of light transports, and the real light paths can be estimated from the Monte Carlo simulations provided that an appropriate tissue model is established.

2.2. Image reconstruction algorithm

We adopted the NL algorithm for both BFI calculations with DCS and BFI imaging with DCT. Unlike the conventional analytical solution and finite element method (FEM), the NL algorithm aims not to seek solutions for correlation diffusion equation. Instead, this approach combines the integral form of the light electric field temporal autocorrelation function $g_1(\tau)$ with the Nth-order Taylor polynomials, and the tissue heterogeneity and irregular geometry are fully taken into consideration through the photon trajectory information. Suppose there are M light sources (1st, ..., Mth) emitting the photons into the tissue, and there are J detectors (1st, ..., Jth) receiving the photons that are escaping out from the tissue. The target tissue is spatially divided into n elements. The collected optical signals (i.e., $g_2(\tau)$) was firstly converted into the light electric field autocorrelation functions ($g_1(\tau)$) via Siegert relation [16]. The $g_1(\tau)$ function collected at (m th, j th) S-D pair can be regarded as the integral of the autocorrelation attenuation of a single photon packet through different elements, as shown in Eq. (1) [24]:

$$\begin{aligned}
 g_1(m, j, \tau) &= \frac{\langle E(m, j, 0)E^*(m, j, \tau) \rangle}{\langle |E(m, j, 0)|^2 \rangle} \\
 &= \int_0^\infty P(m, j, s_1, \dots, s_n) \exp\left(-\frac{1}{3} \sum_{i=1}^n k_0^2(i) \langle \Delta r_i^2(\tau) \rangle \frac{s_i}{l_i^*}\right) ds_1, \dots, ds_n \quad (1) \\
 &= \int_0^\infty P(m, j, s_1, \dots, s_n) \exp\left(-2 \sum_{i=1}^n k_0^2(i) \alpha D_B(i) s_i \mu_s'(i) \tau\right) ds_1, \dots, ds_n
 \end{aligned}$$

where $P(m, j, s_1, \dots, s_n)$ is the normalized distribution of the photon path length detected on the n elements, $k_0(i)$ is the light wave vector amplitude of the i th element, and the random walking

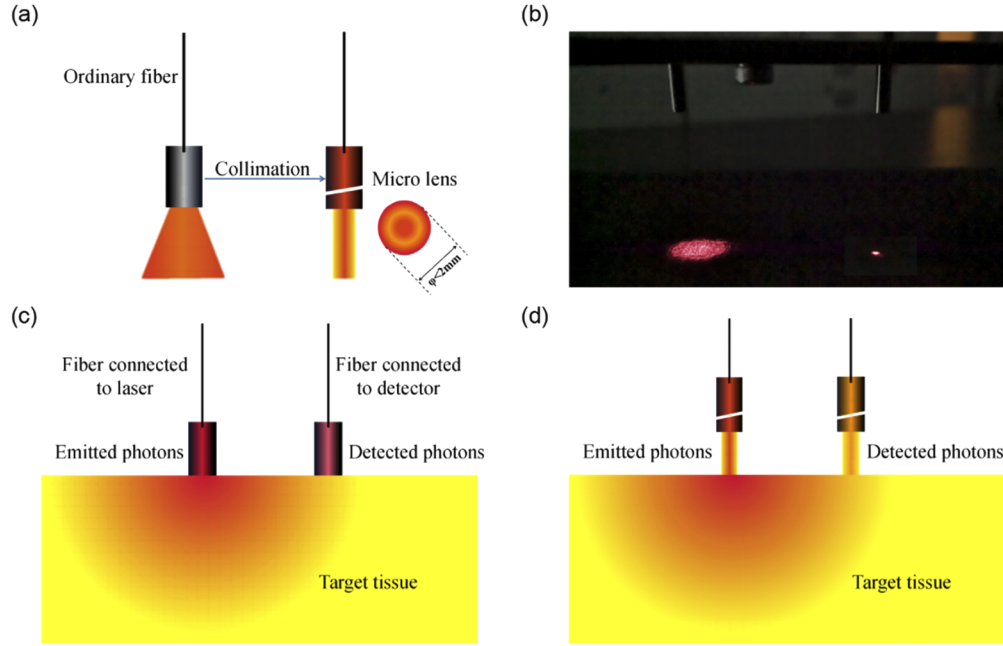


Fig. 2. (a) The schematic diagram of the optical path of an ordinary fiber (without collimating) and a collimating micro lens fiber. (b) Spot size measured with an ordinary fiber (without collimating) and a collimating micro lens fiber respectively, at a working distance of 3 cm. (c) The placement of the contact fiber on the target tissue. (d) The focus of the collimating micro-lens fiber over the target tissue (only one S-D pair is exhibited for clarity).

step length of the i th photon is equal to $1/\mu_s'$ (μ_s' is the reduced scattering coefficient of the i th element). $\langle \Delta r^2(\tau) \rangle$ is the mean square displacement of the moving scattering, and τ is the delay time of the autocorrelation function. According to different physical models, there will be different mathematical forms of red blood cell (RBC) movements (i.e., the blood flow model). In the case of Brownian motions, $\langle \Delta r^2(\tau) \rangle = 6\alpha D_B \tau$. Here the variable $\alpha D_B(i)$ represents the blood flow index (BFI) of the i th element.

On the other hand, the continuous function $g_1(m, j, \tau)$ can be written as a Nth-order Taylor polynomial in the following form [12]:

$$g_1(m, j, \tau) = g_1(m, j, 0) + g_1^{(1)}(m, j, 0)\tau + \sum_{k=2}^N \frac{g_1^{(k)}(m, j, 0)}{k!} \tau^k + \frac{g_1^{(N+1)}(m, j, \xi) \tau^{N+1}}{(N+1)!}, \quad (0 < \xi < \tau) \quad (2)$$

$$g_1(m, j, \tau) - 1 = \tau \sum_{i=1}^n B(m, j, i) \alpha D_B(i) \quad (3)$$

$$g_1(m, j, \tau) - 1 = \sum_{k=2}^N \frac{\sum_{q=1}^Q w(q, m, j) \left(-2 \sum_{i=1}^n k_0^2(i) \alpha D_B(i) s(i, q, m, j) \mu_s'(i) \right)^k}{k!} \tau^k + \tau \sum_{i=1}^n B(m, j, i) \alpha D_B(i) \quad (4)$$

where

$$B(m, j, i) = \sum_{q=1}^Q -2w(q, m, j)k_0^2(i)s(i, q, m, j)\mu'_s(i) \quad (5)$$

The variable $w(q, m, j)$ is termed as the photon weight, and it is also a discrete form of $P(m, j, s_1, \dots, s_n)$. $P(m, j, s_1, \dots, s_n)$ is the path length (s_1, \dots, s_n) of the q th photon ($q = 1, \dots, Q$) over the n elements. $s(i, q, m, j)$ represents the i th path length corresponding to the q th photon packet at the (m, j) S-D pair. Both $w(q, m, j)$ and $s(i, q, m, j)$ can be estimated from photon Monte Carlo simulation of heterogeneous tissues with arbitrary geometries.

In order to facilitate the calculation, according to the relation: $h = j + (m-1)J$, the two-dimensional matrix (m, j) is converted into a one-dimensional matrix h ($h = 1, \dots, MJ$), and then we define some variables:

$$A(h, i) = B(m, j, i) \quad (6)$$

$$\alpha D_B = [\alpha D_B(1), \alpha D_B(2), \dots, \alpha D_B(n)]^T \quad (7)$$

A is an $MJ \times n$ matrix, and αD_B is an $n \times 1$ matrix. When the order $N=1$, the unknown variable αD_B only appears on the right side of Eq. (3). Therefore, Eq. (3) can be written as the following equation:

$$g_1(h, \tau) - 1 = \tau \sum_{i=1}^n B(m, j, i) \alpha D_B^{(1)}(i) = \tau \sum_{i=1}^n A(h, i) \alpha D_B^{(1)}(i) = \tau (A * \alpha D_B^{(1)}) \quad (8)$$

The combined term $A * \alpha D_B^{(1)}$ is the slope of the linear regression between τ and $g_1(h, \tau) - 1$, which can be rewritten as:

$$A * \alpha D_B^{(1)} = Sl \quad (9)$$

Once the slope (Sl) is determined by linear regression between τ and $g_1(h, \tau) - 1$ data, a specific image reconstruction algorithm can be used to calculate the unknown ($\alpha D_B^{(1)}$) according to Eq. (9).

When the order $N > 1$, the unknown variable αD_B appears on both sides of Eq. (4). Therefore, the calculation of blood flow index (BFI) is performed according to an iterative process:

$$g_1(h, \tau) - 1 = \sum_{k=2}^N \frac{\sum_{q=1}^Q w(q, h) \left(-2 \sum_{i=1}^n k_0^2(i) \alpha D_B^{(N-1)}(i) s(i, q, h) \mu'_s(i) \right)^k}{k!} \tau^k \quad (10)$$

$$= \tau \sum_{i=1}^n A(h, i) \alpha D_B^{(N)}(i) = \tau (A * \alpha D_B^{(N)})$$

$$A * \alpha D_B^{(N)} = Sl^{(N)} \quad (11)$$

For the DCT imaging framework of the NL algorithm, the main calculation process includes obtaining the slope through linear regression and solving the linear equations to reconstruct the BFI value (i.e., αD_B). The linear regression between the delay time (τ) and the modified autocorrelation function [left side of Eq. (4)] can be easily achieved by the least-square method. Generally, more iteration would lead to more accurate outcomes. In phantom experiments, we used 48 S-D pairs, which is far less than the number of measured tissue voxels (i.e., 2250 unknown αD_B). This leads to severe ill-condition in Eqs. (9) and (11). Therefore, design of constraint and regularization methods to solve linear equations is the major challenge for implementation of BFI image reconstruction.

Previously, a hybrid algorithm that combines the total variation (TV) and split-Bregman were proposed by us. This hybrid algorithm, namely Bregman-TV, was used to perform BFI image

reconstruction. Here, Bregman's algorithm provides a solution for non-differentiable equations. The TV algorithm can make non-edge areas more uniform, while well retaining the edges. In Eq. (9) and Eq. (11), let $v = \alpha D_B^{(N)}$, $b = Sl^{(N)}$, and the minimization problem of Bregman-TV imaging framework is expressed in Eq. (12):

$$\begin{aligned} v^* = \arg \min & \|v\|_{TV} + \frac{\mu}{2} \|Av - b\|_2^2 \\ \text{s.t. } & v_i \geq 0 \quad (i = 1, \dots, n) \end{aligned} \quad (12)$$

TV regularization aims to sparsely represent an image by minimizing the L_1 norm of the gradient magnitude of the image. As for solving the TV minimization problem, the split-Bregman algorithm is proven to be an effective method [12].

2.3. Phantom configuration for DCS and DCT measurement

The liquid phantom experiments are commonly used in DCS and DCT studies for standard validation. Details of the phantom procedures were reported elsewhere [11,13,16]. Briefly, the liquid phantom, consisting of distilled water, India ink (Chenguang Inc., China) and Intralipid solution (30% solution, Huarui. Inc., China), are contained in a glass rectangular aquarium. The India ink is used to create the light absorption, and the Intralipid particles are used to create the light scattering and mimic the RBC movements in the phantom. With proper amount of ink solution and Intralipid solution being added, the optical properties of the liquid phantom reach $\mu_a = 0.05 \text{ cm}^{-1}$ and $\mu_s' = 8.0 \text{ cm}^{-1}$, which match the optical parameters of human tissues.

2.3.1. The liquid phantom with flowing anomaly

As the initial procedure of system validation, the FA-nc system was used to measure the $g_2(\tau)$ curves from the liquid phantom, with aim to assess the quality of DCS signals. The detailed experimental configuration is shown in Fig. 3(a). To manipulate the flow speed in the phantom, an apparatus of transparent thin flat tube was designed and mounted on the aquarium. As shown on Fig. 3(b), the embedded flat glass tube was fixed at 5 mm below the surface of the liquid phantom. The tube was filled with the phantom solution, maintaining the same optical property inside and outside of tube. A syringe pump was used to manipulate the flow rate of liquid in the glass tube, creating the flow anomaly in the phantom. Thereafter, the flow rate in glass tube was manipulated by varying the syringe pump speed in the following steps: 0mL/H, 100mL/H, 200mL/H, 300mL/H, 400mL/H, 500mL/H. The DCS signals were longitudinally collected during the entire period of phantom experiment.

The rectangular shape of flat tube provides a relatively homogeneous flow within the tube, with aim to match the DCS measurement which averages the flows over the region covered by the fiber array. For the purpose of DCT imaging, however, a cylinder tube [Fig. 3(c)] is designed to create a spatial contrast of flow between the tube and the background (i.e., the liquid phantom in aquarium). The approaches to manipulate the flow inside cylinder tube by syringe pump is the same as those for rectangular tube, except that the optical signals collected by the fiber array are used for DCT imaging, instead for DCS measurements.

2.3.2. The liquid phantom with solid anomaly

To comprehensively valuate the capacity of FA-nc system for DCT flow imaging, we also set up a solid anomaly (i.e., zero flow) as a representative of lower flow than the background. The basic phantom configuration is similar to that for flowing anomaly, except embedding a solid rectangular-shape anomaly instead of a tube filled with liquid phantom. The anomaly was made of solid phantom, with same optical properties (μ_a and μ_s') as the liquid phantom. The solid anomaly, at size of 15mm×5mm×5mm, are embedded in the phantom at the 5 mm below the

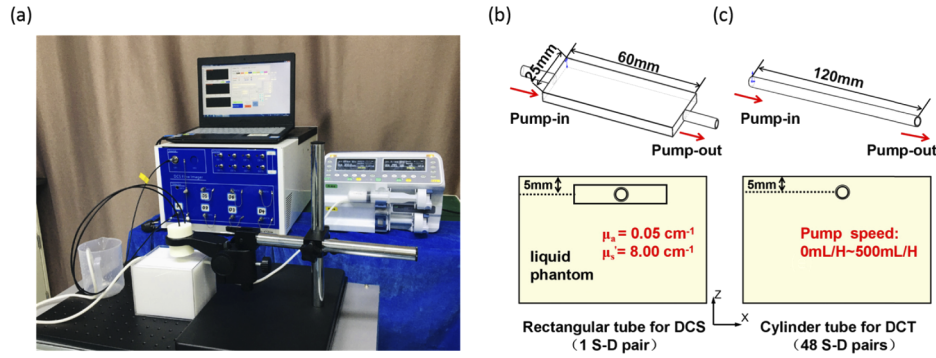


Fig. 3. (a) FA-nc system for measurement of the phantom BFI that is manipulated by syringe pump. The rectangular shape (b) and cylinder shape (c) of transparent thin tube, both of which are filled with liquid phantom for creating the flow contrast inside and outside of tube. The rectangular tube and cylinder tube are designed for DCS measurement and DCT imaging respectively.

liquid surface, as shown in Fig. 4(a). A very thin needle, with one end being inserted into a base placed on the bottom of the aquarium, was used to fix the solid anomaly with its other end.

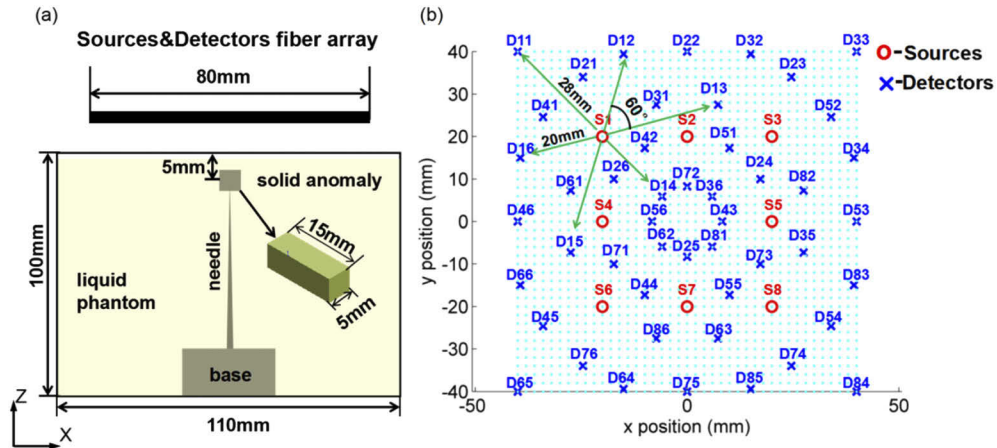


Fig. 4. (a) The phantom configuration with a solid anomaly embedded at 5 mm below the liquid surface. (b) The arrangement of 8 sets of S-D pairs on FA-nc probe. The labels for each set of S-D pairs are listed in Table 1.

2.3.3. S-D array for FA-nc system

The detailed S-D array for FA-nc system is depicted in Fig. 4(b). There are a total of 8 sets of S-D pairs in the array, covering the entire region of optical measurements. Each set include one source and six detectors whose specific labels are listed in Table 1. The reason for this design is to balance the measurement direction, S-D separation and the covering sub-regions. As such, the condition number of matrix in NL algorithm [Eqs. (9) and (11)] remain normal which ensures the robust reconstruction of flow imaging. Specifically, each source location is surrounded by six detector locations at the S-D separation of 2.0 cm or 2.8 cm. The sources and detectors are mostly cross-arranged, which is more flexible when compared with the rotated-scanning of the line-shape fiber array that is dominantly adopted. With the sequentially light switching for 8

times by the optical switch, a 48 (6×8) times of data acquisitions are attained, at a sampling time of 1 second for each switch. The integration time for each set of source-detector (i.e., one source and six detectors) is 1 second, similar to that for diffuse correlation spectroscopy (DCS). Hence, the SNR with 1-second integration time is sufficient for both phantom and human arm experiments. As such, the measurement time for a complete DCT data acquisition is around 10 seconds (including 8 set of S-D measurement time and 8 times of switching time). Although the CCD-based DCT system would greatly accelerate the measurement speed, the SNR is much lower, limiting the penetration depth.

To comply with the NL algorithm for DCT imaging, photon Monte Carlo simulation was performed on the volume with size of 8cm×8cm×3cm. During this process, both the rectangular and cylinder shapes of glass tube were taken into account when establishing the geometrical model for photon Monte Carlo simulation. Specifically, a refractive index of 1.5 and zero values of flow, absorption and scattering coefficients were assumed for glass tubes in the geometrical model. The Nth-order linear algorithm (NL) incorporates these information for image reconstruction and minimizes the boundary effect. The simulation outcomes, especially the photon path lengths and weight factors, are incorporated with the optical signals ($g_1(\tau)$) to form the imaging framework [i.e., Eqs. (10)-(12)]. By using the strategy of image reconstruction (i.e., Bregman-TV) illustrated in Section 2.2, the BFI imaging was obtained and evaluated.

2.4. Human experiment of arterial occlusion for DCS and DCT on human forearm

The human experimental protocol was approved by the Ethics Committee of North University of China. All of the seven volunteers participating in the study have signed the consent form before the measurements. For the *in vivo* measurement, subject laid supine on the table with the right arm relax on the table. An elastic strap was used to stabilize the arm in the middle. Besides, we monitored the entire process of optical measurements and excluded all of the data that might be affected by motion artifacts. The details of source-detector separation are also illustrated in Fig. 4(b). A cuff tourniquet was placed on the upper arm. For the purpose of comparison, the FA-nc system and a conventional contact probe were focused/placed on the surface of right forearm. The integration time of DCS is set as 1 second for both contact and noncontact studies. The laser was controlled by the optical switch to emit light into noncontact (FA-nc) and contact tissue area alternately, at the sampling time of 2 seconds, so as to avoid the light interference between the two measurements. After 60-second baseline measurement, the cuff tourniquet was inflated to 230 mmHg, with aim to temporally block the arterial flow into forearm muscles for 150 seconds. The cuff pressure was then released and the optical signals were collected for another 90 seconds. Throughout the 5-minute measurement, the subject remained still to minimize the motion artifacts on the DCS/DCT measurements.

3. Results

At the largest source-detector separation (i.e., 3.0 cm), the light intensity derived from the noncontact probe is around 60 kcps in liquid phantom and 50 kcps in human arm tissue. These integration time and light intensity are sufficient for the Nth-order linear algorithm to generate stable slopes of the linear regression as well as flow imaging. The light intensity derived from the contact probe are at the same order as that derived from the noncontact probe.

3.1. Phantom experiment for DCS and DCT measurement

The results of phantom experiments for DCS measurements are shown in Fig. 5. According to the Siegert relation [16], the ideal value for the first data point of $g_2(\tau)$ curves is 1.50, which matches well with the measured values from the phantom experiments [between 1.46 and 1.50, see Fig. 5(a)]. These observations indicate that the $g_2(\tau)$ curves collected by the FA-nc probe are typical, with little effects from the ambient light. When subjected to speed manipulation by

syringe pump, the flow inside the glass tube varies accordingly. As illustrated in Fig. 5(b), the BFI (i.e., αD_B) values extracted from the autocorrelation data increase linearly with the pump speed, with excellent correlations ($R^2=0.998$, $p<10^{-5}$). These outcomes verify the capacity of FA-nc system for minimizing the light interference between sources and detectors as well as yielding high quality of autocorrelation curves.

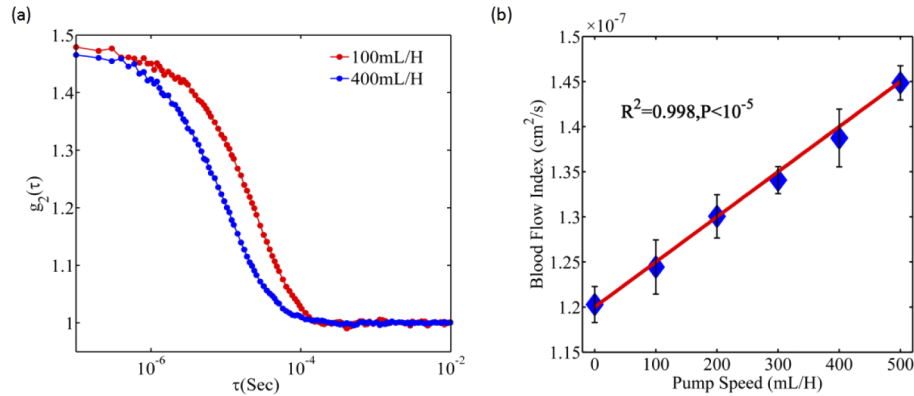


Fig. 5. (a) The $g_2(\tau)$ curves measured directly from the FA-nc system, at pump speed of 100ml/H and 400 ml/H respectively. (b) The linear regression between the pump speed and blood flow index derived from FA-nc system. The data were averaged over 10 times of repeated measurements and presented as mean \pm SD.

Figures 6(a) and 6(c) shows respectively the 3D flow imaging of solid anomaly and flowing anomaly within the transparent tube (at pump speed of 400ml/H) that were derived from the FA-nc-DCT system, wherein the image reconstruction was implemented by the NL imaging framework. Figures 6(b) and 6(d) shows the 2D cross-section views (i.e., X-Y plane) of anomaly imaging at the depths of 3 mm, 5 mm and 7 mm below the phantom surface, respectively, which can illustrate both solid anomaly and the flowing anomaly within the transparent tube. The location and size of anomaly match exactly with the experimental configuration.

3.2. Human experiment of arterial occlusion for DCS and DCT on human forearm

Figure 7(a) shows the representative time course of blood flow changes throughout the manipulation protocol of arterial occlusion, measured by the contact and FA-nc systems respectively. As clearly seen, the temporally arterial occlusion by cuff tourniquet causes a sharp and large decrease in BFI value. Upon the release of cuff tourniquet, there is a hyperemia response (i.e., the BFI promptly surges into the peak value), followed by the gradual recovery to its baseline. The BFI responses to the arterial occlusion measured by the FA-nc probe (red curve) is very similar to that measured by contact probe (blue curve), with the average difference small than 5%. Note that the focusing areas by the two probes are 2 cm apart on the forearm surface. The small difference between the two measurements may due to the tissue heterogeneous response to the ischemic muscles. On average ($n=7$), the BFI declines caused by arterial occlusion is $65.7 \pm 2.43\%$ and $69.0 \pm 9.51\%$ (mean \pm SD) measured by noncontact and contact probe respectively [Fig. 7(b)]. These observations demonstrate that the FA-nc measurements are stable and little affected by the ambient light as well as the possible trembling of the human body.

Figure 8 shows the BFI imaging of skeletal muscle at normal (before occlusion) and ischemic status (during occlusion) respectively, both of which are reconstructed by FA-nc-DCT system and NL imaging framework. At either status, the BFI value are evenly distributed over the target tissue, with small spatial variation. However, a large imaging contrast is clearly seen between the

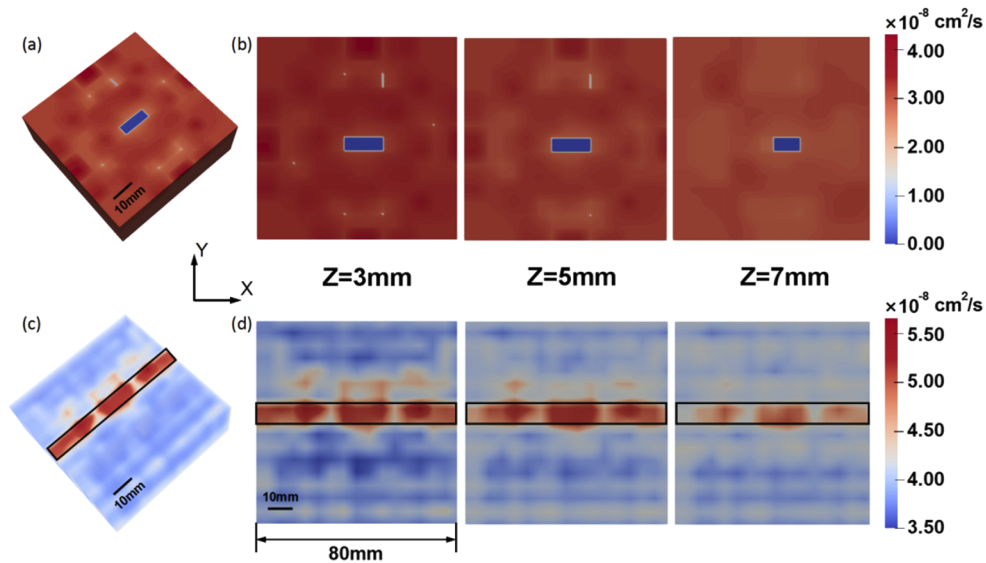


Fig. 6. (a) The 3D imaging of liquid phantom with a solid anomaly. (b) The 2D cross-section views (i.e., X-Y plane) of solid anomaly at the depths of 3, 5 and 7 mm below the phantom surface. (c) The 3D imaging of liquid phantom with a flowing anomaly within the transparent tube. (d) The 2D cross-section views (i.e., X-Y plane) of the flowing anomaly within the transparent, at the depths of 3, 5 and 7 mm below the phantom surface. Note that the target anomaly in (c) and (d) are outlined in black for better illustration.

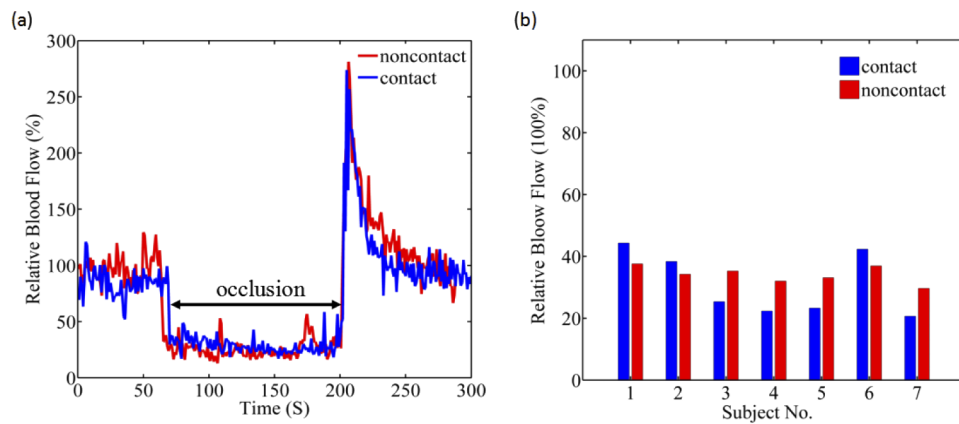


Fig. 7. (a) The time-course changes of blood flow throughout the arm cuff occlusion, measured by contact and noncontact probe (i.e., FA-nc system) respectively. (b) The relative blood flow during cuff occlusion measured by contact and noncontact probes in all of the seven healthy subjects, in which the baseline flow is set as 100% before occlusion.

two states (normal and ischemic), which coincides with the DCS measurements subjected to the same physiological protocol.

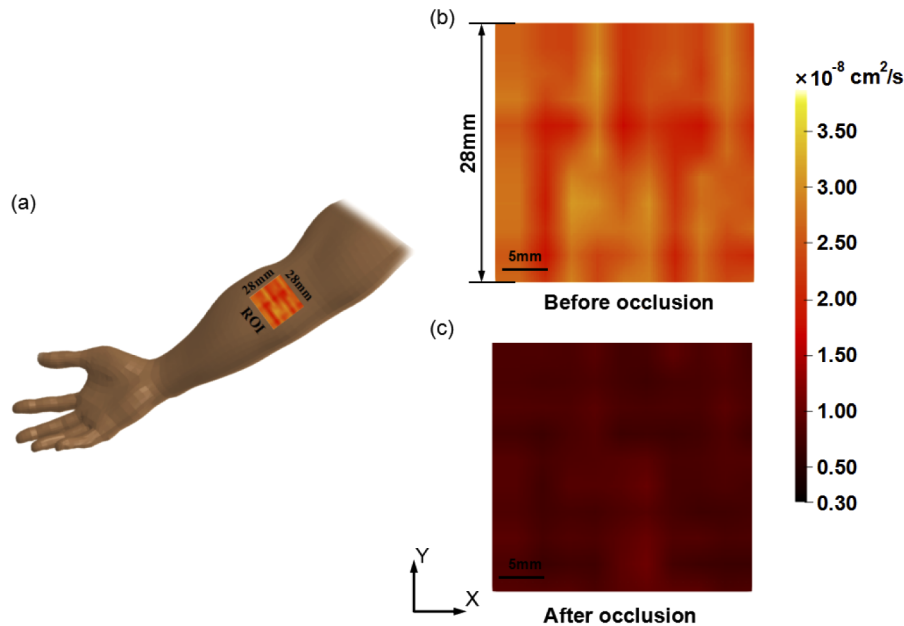


Fig. 8. The BFI imaging of skeletal muscle at normal (before occlusion) and ischemic status (during occlusion) respectively, reconstructed by FA-nc-DCT system. (a) BFI imaging shown on the forearm. (b) The BFI imaging at normal status (c) The BFI imaging at ischemic status.

4. Discussion and conclusions

Blood flow is a critical physiological parameter for the diagnosis of many diseases. However, the technologies currently available for assessment of the blood flow at microvasculature level is limited. The ultrasound Doppler routinely used in clinic can only measure the blood flow of the major vessels [25]. The imaging modality of arterial spin labeling-magnetic resonance imaging (ASL-MRI) relies on heavy and expensive instruments, and it thus not feasible for early diagnosis and bed-side monitoring [26]. Other modalities such as laser Doppler or laser speckle flowmetry, can only assess the blood flow at superficial tissues, up to 2 mm [27,28]. There is an urgent clinical need for portable and inexpensive measurement and imaging of the microvasculature blood flow in deep tissues. In recently years, the DCS/DCT have been rapidly developed to assess the tissue blood flow at relatively large depths (up to several centimeters). The contact probe was primarily use for DCS measurement due to multiple advantages such as easy-to-setup and less sensitivity to the ambient light and motion artifacts. In some situations that tissue surface cannot be touched or deformed (e.g., wound and ulcer tissues), the noncontact probe should be used, primarily for DCT studies. For example, a camera-based noncontract probe was used to focus all of source and detector fibers on the tissue surface via an identical lens system. However, the aberration effects limit the FOV, precluding the use of this sort of probe for large human tissues. To overcome this limit, a line-shape probe with independent lens systems was designed to separate the optical path of sources and detectors. The line-shape probe enables large FOV through rotated-scanning over the target tissue. Nevertheless, the scanning pattern prolongs the measurement time and increase the instability. On the other hand, the use of regular combined

lens for both source and detector makes it difficult to achieve the small S-D separation (e.g., <1 cm), which, however, is important for algorithm optimization of image reconstruction.

In this study, we designed a new noncontact probe for DCT based on micro lens collimating fiber array (i.e., FA-nc-DCT). Unlike the previous camera-based and line-shape probes, we do not use the regular combined lens to collimate and focus the optical paths, but manage to couple micro lens system in front end of each optical fiber. This unique design significantly reduces the S-D separation and allows for flexible positioning of the S-D fiber array. Moreover, an 8×8 optical switch is designed to rapidly distribute the light to different S-D locations without the effects from scanning vibrations. The collimating micro-lens fiber array would allow for the arbitrary arrangement of the source-detector (S-D) pair within the entire FOV region. Hence, this pattern can be more efficiently integrated with the Nth-order linear (NL) algorithm that was previously created by us. By contrast, the scanning-based system is similar to the duplication of one set of S-D arrangement (e.g., a source and six detectors) among different locations or directions, i.e., moving this arrangement from one location/direction to another location/direction. Hence, the flexible S-D arrangement is limited. The use of optical switch avoids the influence of motion artifacts caused by the mechanical scanning. Additionally, the individual fiber collimating minimizes the light interference between the source and detector that is caused by any form of shared lens. Although the form of serial data collection by optical switch lowers down the imaging speed, it greatly reduces the cost of hardware (i.e., the number of lasers and APDs). Compared with spatial scanning (e.g., around 20 seconds for each step of scanning [11]), the optical switching is much faster (e.g., 10 milliseconds for each switching in this study). We are trying to denoise the optical signals meanwhile reducing the measurement time within each switch cycle. This is a way to speed up the data collection and will be one part of our future works.

For DCT studies, the optical measurements (i.e., number of S-D pairs) are far less than the imaging voxels [i.e., the elements in Eqs. (4)–(11)], causing severe ill-conditions in mathematics. Hence, optimization of reconstruction algorithm is critical in order to improve the flow imaging quality. Recently, we developed an DCT imaging framework based on Nth-order linear (NL) algorithm [12], which permits fully utilization of the autocorrelation data, hence more robust to the data noise. The advantages of the NL algorithm over the conventional FEM approach were confirmed through extensive computer simulations and phantom experiments [29]. Further optimization of NL algorithm requires flexible arrangement of S-D fiber array, which could be achieved by the FA-nc system, rather than the current line-shape strategy that strictly separates the optical paths of sources and detectors for large FOV.

Furthermore, different size of ROI was selected for the phantom experiment and human cuff occlusion experiments. Larger ROI is selected for phantom experiment because the phantom container has larger area and rectangular shape. By contrast, the human arm has smaller area and larger curvature. Hence the smaller ROI on arm is selected to match the square-shape probe. The optical properties used for phantom and human arm are the same (i.e., $\mu_a = 0.05\text{cm}^{-1}$ and $\mu_s' = 8.0\text{cm}^{-1}$), except with distinct geometrical models. Specifically, a rectangular geometry was established for phantom experiment, while a cylinder geometry was established for human arm. As mentioned in our previous studies [12,24], the Nth-order linear algorithm would account for the individual geometry and well solve the issues of tissue curvature.

The FA-nc system for minimizing the light interference between the sources and detectors were firstly verified by DCS measurements on liquid phantom and human experiments. The typical curves of light autocorrelation ($g_2(\tau)$) were generated [Fig. 5(a)], indicating that the DCS signals are little affected by the FA-nc probe. Additionally, the excellent correlations ($R^2=0.998$, and $p<10^{-5}$) between the BFI values in the glass tube and pump speed also meet our expectation. As for the practical applications in human tissues, typical blood flow responses to transient muscle ischemia and reperfusion were observed, which also coincides with the

concurrent blood flow measurements with contact DCS probe. For application of FA-nc system on DCT, the NL imaging framework was adopted to process the autocorrelation data, and the rectangular-shape flow anomaly was successfully reconstructed. In addition, the location and edges are well reserved. These observations demonstrate that the FA-nc system has the capacity to accurately detect and localize flow anomaly. Moreover, the FA-nc-DCT for blood flow imaging of the normal and ischemic human skeletal muscles were also clearly observed.

Despite of the merits, the current FA-nc probe, along with the optical switch, permits only forming a 6×8 S-D array. Accordingly, the flow imaging with voxel size of 2 mm is attained. High density of S-D array is required for further improving the image quality and elevating the spatial resolution. The high density of S-D array would be achieved by micro-scanning of the fiber-array in two perpendicular directions, without increase the instrumentation costs. Besides, the FA-nc system could be comprehensively applied on various clinical studies, which is also the subject of future works.

According to the physical principle, the microvascular flow (measured by DCS/DCT) is much slower than the flow rate by syringe pump. Nevertheless, it is reported that the DCS/DCT flow is proportional to the pump speed [11]. The pump speed of 400ml/h was adopted in this study for better illustration. Our previous study has shown that the pump speed of 200ml/h is still detectable by the contact system and Nth-order linear (NL) algorithm [29]. Nevertheless, determination of the minimal detectable flow is an interesting task for improving the DCT technique. A potential solution is combining the galvanometer-based scanning with optical switch, which would greatly increase the DCT measurement density, yielding high-resolution imaging of tissue blood flow. This combination will be a main direction of our future study.

In summary, a novel noncontact system based on collimating micro lens fiber array (FA-nc) was designed by us for DCT blood flow imaging. With a micro-lens installed on each fiber, the optical path from individual fiber was collimated and focused on the tissue surface without sharing an identical lens system among the sources and detectors. The FA-nc system for minimizing the light interference were validated on the speed-varied liquid phantom and human experiments. Moreover, the integration of flexible S-D array and the NL algorithm has been extensively proven to be effective for 3D imaging of both phantom and *in vivo* tissue flow. The accurate reconstruction outcomes demonstrate the great potential of FA-nc-DCT system for future blood flow imaging that are associated with disease diagnosis and therapeutic assessment.

Funding. Shanxi Provincial Key Research and Development Project (201903D121149); Natural Science Foundation of Shanxi Province (201901D111153); National Natural Science Foundation of China (61671413, 61771433); National Key Scientific Instrument and Equipment Development Projects of China (2014YQ24044508); OIT Program of Shanxi Province and Department of Education, Shanxi Province (2020SY363, 2020SY364).

Disclosures. The authors declare that there are no conflicts of interest related to this article.

References

1. Y. Shang, T. Li, and G. Yu, "Clinical applications of near-infrared diffuse correlation spectroscopy and tomography for tissue blood flow monitoring and imaging," *Physiol. Meas.* **38**(4), R1–R26 (2017).
2. T. Durduran, R. Choe, W. B. Baker, and A. G. Yodh, "Diffuse optics for tissue monitoring and tomography," *Rep. Prog. Phys.* **73**(7), 076701 (2010).
3. D. A. Boas, L. E. Campbell, and A. G. Yodh, "Scattering and imaging with diffusing temporal field correlations," *Phys. Rev. Lett.* **75**(9), 1855–1858 (1995).
4. D. A. Boas, S. Sakadzic, J. Selb, P. Farzam, M. A. Franceschini, and S. A. Carp, "Establishing the diffuse correlation spectroscopy signal relationship with blood flow," *Neurophotonics* **3**(3), 031412 (2016).
5. C. Cheung, J. P. Culver, K. Takahashi, J. H. Greenberg, and A. G. Yodh, "In vivo cerebrovascular measurement combining diffuse near-infrared absorption and correlation spectroscopies," *Phys. Med. Biol.* **46**(8), 2053–2065 (2001).
6. T. Durduran, R. Choe, G. Yu, C. Zhou, J. C. Tchou, B. J. Czerniecki, and A. G. Yodh, "Diffuse optical measurement of blood flow in breast tumors," *Opt. Lett.* **30**(21), 2915–2917 (2005).
7. R. Choe, M. E. Putt, P. M. Carlile, T. Durduran, J. M. Giammarco, D. R. Busch, K. W. Jung, B. J. Czerniecki, J. Tchou, M. D. Feldman, C. Mies, M. A. Rosen, M. D. Schnall, A. DeMichele, and A. G. Yodh, "Optically measured microvascular blood flow contrast of malignant breast tumors," *Plos One* **9**(6), e99683 (2014).

8. C. Zhou, G. Yu, D. Furuya, J. H. Greenberg, A. G. Yodh, and T. Durduran, "Diffuse optical correlation tomography of cerebral blood flow during cortical spreading depression in rat brain," *Opt. Express* **14**(3), 1125–1144 (2006).
9. J. P. Culver, T. Durduran, T. Furuya, C. Cheung, J. H. Greenberg, and A. G. Yodh, "Diffuse optical tomography of cerebral blood flow, oxygenation, and metabolism in rat during focal ischemia," *J. Cereb. Blood Flow Metab.* **23**(8), 911–924 (2003).
10. C. Huang, D. Irwin, Y. Lin, Y. Shang, L. He, W. K. Kong, J. Luo, and G. Yu, "Speckle contrast diffuse correlation tomography of complex turbid medium flow," *Med. Phys.* **42**(7), 4000–4006 (2015).
11. Y. Lin, C. Huang, D. Irwin, L. He, Y. Shang, and G. Yu, "Three-dimensional flow contrast imaging of deep tissue using noncontact diffuse correlation tomography," *Appl. Phys. Lett.* **104**(12), 121103 (2014).
12. X. Zhang, Z. Gui, Z. Qiao, Y. Liu, and Y. Shang, "Nth-order linear algorithm for diffuse correlation tomography," *Biomed. Opt. Express* **9**(5), 2365–2382 (2018).
13. P. Zhang, Z. Gui, G. Guo, and Y. Shang, "Approaches to denoise the diffuse optical signals for tissue blood flow measurement," *Biomed. Opt. Express* **9**(12), 6170–6185 (2018).
14. M. Zhao, S. Mazdeyasna, C. Huang, N. Agochukwu-Nwubah, A. Bonaroti, L. Wong, and G. Yu, "Noncontact speckle contrast diffuse correlation tomography of blood flow distributions in burn wounds: a preliminary study," *Mil Med.* **185**(Supplement_1), 82–87 (2020).
15. Y. Shang, Y. Zhao, R. Cheng, L. Dong, D. Irwin, and G. Yu, "Portable optical tissue flow oximeter based on diffuse correlation spectroscopy," *Opt. Lett.* **34**(22), 3556–3558 (2009).
16. D. Irwin, L. Dong, Y. Shang, R. Cheng, M. Kudrimoti, S. D. Stevens, and G. Yu, "Influences of tissue absorption and scattering on diffuse correlation spectroscopy blood flow measurements," *Biomed. Opt. Express* **2**(7), 1969–1985 (2011).
17. Y. Lin, L. He, Y. Shang, and G. Yu, "Noncontact diffuse correlation spectroscopy for noninvasive deep tissue blood flow measurement," *J. Biomed. Opt.* **17**(1), 010502 (2012).
18. L. He, Y. Lin, C. Huang, D. Irwin, M. M. Szabunio, and G. Yu, "Noncontact diffuse correlation tomography of human breast tumor," *J. Biomed. Opt.* **20**(8), 086003 (2015).
19. C. Huang, D. Irwin, M. Zhao, Y. Shang, N. Agochukwu, L. Wong, and G. Yu, "Noncontact 3-D speckle contrast diffuse correlation tomography of tissue blood flow distribution," *IEEE Trans. Med. Imaging* **36**(10), 2068–2076 (2017).
20. S. Han, J. Johansson, M. Mireles, A. R. Proctor, M. D. Hoffman, J. B. Vella, D. S. W. Benoit, T. Durduran, and R. Choe, "Non-contact scanning diffuse correlation tomography system for three-dimensional blood flow imaging in a murine bone graft model," *Biomed. Opt. Express* **6**(7), 2695–2712 (2015).
21. S. Han, A. R. Proctor, J. B. Vella, D. S. W. Benoit, and R. Choe, "Non-invasive diffuse correlation tomography reveals spatial and temporal blood flow differences in murine bone grafting approaches," *Biomed. Opt. Express* **7**(9), 3262–3279 (2016).
22. J. Ren, S. Han, A. R. Proctor, D. E. Desa, G. A. Ramirez, V. R. D. Ching-Roa, J. B. Majeski, I. A. Dar, N. E. Barber, A. M. Forti, D. S. W. Benoit, and R. Choe, "Longitudinal 3D blood flow distribution provided by diffuse correlation tomography during bone healing in a murine fracture model," *Photochem. Photobiol.* **96**(2), 380–387 (2020).
23. S. Han, A. R. Proctor, J. Ren, D. S. W. Benoit, and R. Choe, "Temporal blood flow changes measured by diffuse correlation tomography predict murine femoral graft healing," *PLoS One* **13**(5), e0197031 (2018).
24. Y. Shang and G. Yu, "A Nth-order linear algorithm for extracting diffuse correlation spectroscopy blood flow indices in heterogeneous tissues," *Appl. Phys. Lett.* **105**(13), 133702 (2014).
25. S. Bystrom, B. Jensen, M. Jensen-Urstad, L. E. Lindblad, and A. Kilbom, "Ultrasound-Doppler technique for monitoring blood flow in the brachial artery compared with occlusion plethysmography of the forearm," *Scand. J. Clin. Lab. Invest.* **58**(7), 569–576 (1998).
26. G. Yu, T. F. Floyd, T. Durduran, C. Zhou, J. Wang, J. A. Detre, and A. G. Yodh, "Validation of diffuse correlation spectroscopy for muscle blood flow with concurrent arterial spin labeled perfusion MRI," *Opt. Express* **15**(3), 1064–1075 (2007).
27. C. Ayata, A. K. Dunn, Y. Gursoy-Ozdemir, Z. Huang, D. A. Boas, and M. A. Moskowitz, "Laser speckle flowmetry for the study of cerebrovascular physiology in normal and ischemic mouse cortex," *J. Cereb. Blood Flow Metab.* **24**(7), 744–755 (2004).
28. Y. Shang, L. Chen, M. Toborek, and G. Yu, "Diffuse optical monitoring of repeated cerebral ischemia in mice," *Opt. Express* **19**(21), 20301–20315 (2011).
29. J. Zuo, X. Zhang, J. Lu, Z. Gui, and Y. Shang, "Impact of reconstruction algorithms on diffuse correlation tomography blood flow imaging," *IEEE Access* **8**, 31882–31891 (2020).